Nature of sorption of trivalent arsenic on novel iron oxyhydroxide stabilized starch/OMMT composite: A mechanistic approach

P. Gogoi, M. Das, P. Begum and T. K. Maji

ABSTRACT

Materials which are chemically, energetically and operationally acceptable for arsenic water treatment are highly required. In this study a hybrid material (SICC) of aminated starch, oxyhydroxide of iron and OMMT clay has been demonstrated for arsenic treatment. This new material was highly efficient in arsenic water treatment which could reduce arsenic concentration far below detection limits. All binding interactions during material preparation and arsenic sorption were exclusively characterized with FT-IR, XRD and other spectroscopic tools. A molecular modeling on the basis of density functional theory was carried out to verify the above findings. Influence of material dose, treatment time, initial ion concentration, varying temperatures, etc., on extent of sorption was studied in detail. The thermodynamic parameters viz. ΔG (>−11 kJ/mol), ΔH (42.48 kJ/mol), ΔS (177.6 JK^{-1} mol^{-1}) and E a (59.16 kJ/mol) determined the feasibility of the process, its endothermic behavior and most importantly the chemical nature of the sorption accompanied by ion-exchange to some extent. The sorption followed a monolayer chemisorption pattern as determined by the Langmuir model ($R^2 = 0.973$, R L = 0.081) with a $q_{max} = 2.04$ at 303 K. The binding of As(III) on the material was governed by a pseudo second order kinetic model.

Key words | chemisorption, endothermic, feasibility, hybrid material, molecular modeling

P. Gogoi
Department of Chemistry,
Sipajhar College,
Darrang, Assam 784145,
India

M. Das

T. K. Maji (corresponding author)
Department of Chemical Sciences,
Tezpur University,
Assam 784028,
India
E-mail: *tkm@tezu.ernet.in*

P. Begum
Department of Chemistry,
Gargaon College,
Sivasagar, Assam 785686,
India

HIGHLIGHTS

- Properties of the hybrid material were enhanced synergistically.
- Suspended materials were negligibly small in hybrid material.
- Material with 10% clay loading accompanied by Iron(III) oxyhydroxide stabilization was found best in all respects.
- Arsenic on SICC was predominantly chemisorbed accompanied by ion exchange to some extent.
- The sorption process was spontaneous and endothermic in nature.

doi: 10.2166/wh.2021.267

GRAPHICAL ABSTRACT

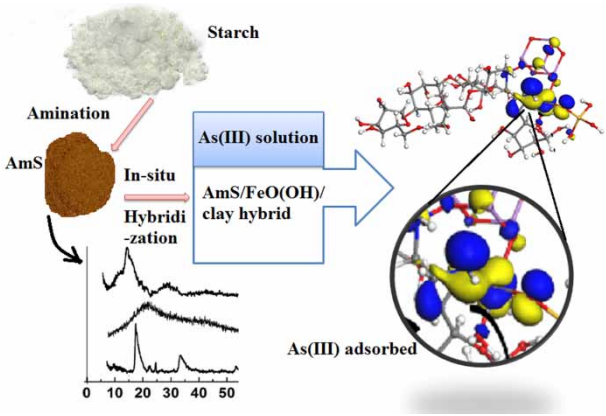

INTRODUCTION

The prevalence of arsenic in drinking water is threatening millions of people's health across the globe every day. Cost effective, simple methods with easily and widely available materials are, therefore, largely required for its remediation. The cutting-edge technologies for remediation of arsenic/other heavy metals from water include sorption over different nanosorbents like carbon, graphene, clay or metal oxide-based nanomaterials (Khodabakhshi *et al.* 2011; Adeleye *et al.* 2016; Gogoi *et al.* 2017a, 2017b, 2017c; Uddin 2017). They have significant sorption capacity due to high porosity, large and active surface, catalytic potential and high reactivity (Hristovski *et al.* 2007; Santhosh *et al.* 2016).

Clay minerals and iron-based nanomaterials have been gaining special attention in this concern owing to their unique arsenic sorption ability. Fe(III)-based sorbents such as magnetite, siderite, hematite, ferrihydrite, etc., have strong affinity and selectivity towards arsenic species (Catalano *et al.* 2011; Gogoi *et al.* 2017a, 2017b, 2017c) Cumbal & Sen Gupta (2005) have reported polymer supported hydrated iron(III) oxide nanoparticles with high arsenic uptake capacity. Iron oxyhydroxide is another iron(III) compound which has outstanding capability to adsorb both As(III) and As(V) species. Activated carbon with iron oxyhydroxide showed good arsenic uptake, though the sorption capacity was not so high (Vitela-Rodriguez & Rangel-Mendez 2013). Arsenic detoxification by clay minerals and their modified forms are also well reported (Mohapatra *et al.* 2007). Srinivasan (2011) has demonstrated the usability of numerous clay minerals found in India in arsenic treatment. Clay such as kaolinite, montmorillonite, etc., and their modified forms have been successfully utilized in the removal of many heavy metals, other contaminants and different forms of arsenic (Lenoble *et al.* 2002; Banu *et al.* 2018). Recently, Cheira *et al.* (2019) have synthesized a new material of bentonite clay for successful removal of certain harmful metal ions. The material retained its efficiency even after six cyclic runs. However, clay minerals are more effective towards positively charged species (Kumar *et al.* 2012). Surfactant modification can alter the nature of clay surface charge to make it a potential binder for negatively charged arsenic species from aqueous solution (Li & Bowman 2001).

However, the free release of nanoparticles to the environment and tendency to agglomerate or probability of structural disintegration during cyclic run can limit their applicability (Lenoble *et al.* 2003; Sepehri & Sarrafzadeh 2018). Many studies have demonstrated the stabilization of the nanomaterials by dispersing them on host materials such as granular activated carbon, cellulose, and biopolymers, etc. (Zhao *et al.* 2011; Gogoi *et al.* 2017a, 2017b, 2017c). The stabilization of mixed metal oxyhydroxide in chitosan biopolymer matrix has been reported in many studies (Zubair *et al.* 2018). Hasan *et al.* (2014) explained the dispersion of FeO(OH) particles in

chitosan matrix for removal of As(III) and As(V) simultaneously where the former themselves can act as crosslinking agent for the matrix. Starch in its pristine form may not be suitable for immobilization of the nanomaterials. Amination of starch increases active binding sites on its backbone. Grafting with glycidyl methacrylate may be an efficient technique to introduce amine functionality in starch biopolymer. The presented work aims to prepare a combined system of clay and aminated starch stabilized with oxyhydroxide and to evaluate its efficiency for successful remediation of trivalent arsenic from aqueous solution.

MATERIALS AND METHODS

Reagents

Starch (extra pure), glycidal methacrylate (GMA), ethylene diamine (EDA), $K_2S_2O_8$, acetone, HCl, $Fe(NO)_3$, and NaOH were purchased from Merck (India). OMMT Nanoclay and sodium (meta) arsenite ($NaAsO_2$) were procured from Sigma Aldrich (USA). All other reagents and chemicals used were of analytical grade.

Preparation of starch/OMMT/FeO(OH) composite (SICC)

It involved three steps:

1. Grafting of starch: Starch and GMA were refluxed together in the presence of redox initiator $K_2S_2O_8$ (6 mmol L^{-1}) under N_2 atmosphere.
2. Amination of grafted starch: Amination was carried out by refluxing with EDA where 0.1 M HCl solutions acted as activator.
3. Preparation of SICC: A suspension of OMMT clay previously dispersed and sonicated was poured into a suspension of dispersed aminated starch under continuous stirring. A 0.06 M $Fe(NO_3)_3$ solution was mixed to it and the final mixture was precipitated with 0.1 M NaOH. It was heated at 50–70 °C and then filtered. The dried and ground powder was sieved to 100 mesh size. Three different variations of materials containing 5, 10 and 20% (w/w) OMMT clay loading were prepared in this way.

Analysis and measurements

Fourier transform infrared spectrophotometer analysis (FT-IR)

A Fourier Transform Infrared Spectrophotometer (FTIR), (NICOLET Impact I-410, USA) was used to evaluate the presence of different functional moiety in different component materials as well as to study their probable interactions in composite formation and the binding process. Infrared radiations in the spectral range of 500–4,000 cm^{-1} were utilized to perform the study.

Thermogravimetric analysis (TGA)

A thermogravimetric analyser (Metler TA 400) was used to record TGA for all the samples at a heating rate of 20 °C/min up to 600 °C under N_2 atmosphere; for understanding thermal degradation pattern for all nanomaterials and polymer composites.

SEM-EDX analysis

Surface morphologies of the prepared composite material were studied with a scanning electron microscope (JEOL 6390LV, Japan). Elemental composition of the samples before and after As(III) treatment was analyzed with the help of an energy dispersive X-ray analyzer (EDX, Japan).

pH measurement

The pH of the arsenic solutions was adjusted using either HCl (0.1 M) solutions and/or NaOH (0.1 M) as and when required and measured using a Cyberscan pH 510 Eutech (USA) instrument.

Atomic absorption spectroscopic analysis (AAS)

An Analyst 200 atomic absorption spectrophotometer (AAS, Perkin Elmer, Swizerland) was used to quantify the As(III) concentration. The measurements were based on integrated absorbance and performed at 193.7 nm by using a quartz tube analyzer (AAS, Perkin Elmer, Switzerland) at an atomization temperature of 2,000 K.

BATCH ADSORPTION EXPERIMENT

A standard stock solution of 1,000 mg/L of As(III) was diluted in steps as required to obtain different standard solutions for batch experiments. Equilibrium adsorption capacity is given in the following equation:

$$q_e = \frac{(C_o - C_e)V}{M} \tag{1}$$

where q_e (mg/g) is the equilibrium adsorption capacity, C_o and C_e are the initial and equilibrium concentration (mg/L), V(L) is the volume and M(g) is the weight of the adsorbent (Table 1).

Kinetics and adsorption isotherm studies were carried out with five different initial concentrations as in the kinetic data table (Table 4). During those studies the adsorbent dose was maintained at 2 g/L.

The separation factor, R_L, which gives an idea about favorability of the adsorption described by the Langmuir equation and is calculated as:

$$R_L = \frac{1}{(1 + bC_\circ)} \tag{2}$$

Sorption is unfavorable if $R_L > 1$, linear if $R_L = 1$, favorable if $0 < R_L < 1$ and irreversible if $R_L = 0$.

Thermodynamics of sorption

Batch experiments were carried out at three different temperatures viz. 303, 308 and 313 K and second order rate constants (k_2) were plotted against 1/T as described by the Arrhenius equation below. From the slope of the straight line activation energy (E_a) was calculated.

$$\ln k_2 = \ln A - \frac{E_a}{RT} \tag{3}$$

where A is Arhenius temperature independent factor. The other thermodynamic parameters, viz. change in Gibbs free energy (ΔG°), enthalpy (ΔH°) and entropy (ΔS°) were evaluated by using the following equations:

$$Kc = \frac{C_A}{C_S} \tag{4}$$

$$\Delta G^o = -RT \ln Kc \tag{5}$$

$$\ln Kc = \frac{\Delta S^o}{R} - \frac{\Delta H^o}{RT} \tag{6}$$

where K_c is the equilibrium constant, C_A is the amount of arsenite (mol/L) adsorbed on the surface of the material; C_S (mol/L) is the amount remaining in the solution.

Computational method

All density functional calculations were performed with the help of the DMol^3 modeling program in which graphical displays were generated using BIOVIA Materials Studio. DMol^3 is a unique quantum mechanical code for molecular DFT calculations which can rapidly perform structure

Table 1 | Kinetic and isotherm models and equations

Kinetic/isotherm models	Expression	Important terms
First order	$\log_{10}(q_e - q_t) = \log_{10} q_e - \frac{k_{ad}}{2.303t}$	q_t – arsenic adsorbed (mg/g) at time t q_e – arsenic adsorbed (mg/g) at equilibrium K_{ad} – first order rate constant (min^{-1})
Second order	$\frac{t}{q_t} = \frac{1}{h} + \frac{t}{q_e}$	q_t, q_e – usual meaning k – second order rate constant (g mg^{-1} min^{-1}) $h = kq_e^2$ (mg g^{-1} min^{-1}) – initial sorption rate.
Langmuir	$\frac{1}{q_e} = \frac{1}{q_m b}\frac{1}{C_e} + \frac{1}{q_m}$	C_e – equilibrium concentration (mg/L) q_m – maximum adsorption capacity (mg/g) b – Langmuir constant
Freundlich	$\ln q_e = \ln k_f + \frac{1}{n}\ln C_e$	k_f (mg/g) – Freundlich constant related to adsorption capacity 'n' is a constant related to energy of intensity of adsorption

optimizations of molecular systems using a numerical radial function (Delley 1990) basis to calculate the electronic properties. The calculations were performed using the generalized gradient approximation (GGA) with Perdew-Wang 1991 (PW91) exchange-correlation functional (Perdew *et al.* 1996; Delley 2000). The van der Waals interactions were taken into consideration while performing theoretical calculations. Dispersive forces, or van der Waals forces, resulted from the interaction between fluctuating multipoles without requiring the overlap of electron densities (Appalakondaiah *et al.* 2012). Therefore, dispersion corrected density functional theory (DFT-D) was adopted using numerical DND (double numerical plus d-functions, with a polarization d-function on all non-hydrogen atoms) basis set for geometry optimization and frequency analysis (Delley 1990; Ortmann *et al.* 2006). The geometries of reactants and the cross-linked product were optimized without imposing any symmetry constraints using all electron spin-unrestricted calculation, indicating an electronically open shell system. For the heavy metals As and Fe, the valence electrons were described by a double numerical basis set with a polarization function and the core electrons were described with local pseudo-potential (VPSR – which includes all electrons explicitly and introduces some relative effects into the core) (Delley 1998; Zhou *et al.* 2007). The structures were fully relaxed and positive vibrational frequencies confirmed the complexes to be at energy minima.

RESULTS AND DISCUSSION

Characterization

FTIR analysis

Figure 1(a)–1(g) represents the FTIR spectra of starch, St-g-GMA, AmS, nanoclay (OMMT), SIC, SICC and ATC respectively. Bands near 3,380–3,450 and 2,930 cm^{-1} in most of the cases were due to –OH and $–CH_2$ stretching vibration respectively. In the case of starch (a) a broad band at 3,410 cm^{-1} corresponding to –OH stretching indicated the presence of a large number of H-bonding. A band near 1,656 cm^{-1} was due to –OH bending mode of vibration. The two bands in the region 1,170 and 1,004 cm^{-1} could be assigned to the C–O bond stretching of the C–O–H group (Kousalya *et al.* 2010).

Grafting with GMA (b) resulted in sharpening of the band due to –OH stretching. This may be due to breakdown of many hydrogen bonded sites during the grafting process. Also, the grafting was accompanied by the appearance of new bands near 1,716 and 1,035 cm^{-1} which could be assigned for C=O and C–O stretching mode of vibrations of newly inserted ester groups respectively. The characteristic band around 1,273 cm^{-1} was due to the characteristic peaks of the epoxy group (Hedin *et al.* 2010). The strong broad band which appeared at 3,383 cm^{-1} (curve c) after amination was mainly due to the –NH stretching vibration (overlapped by OH).

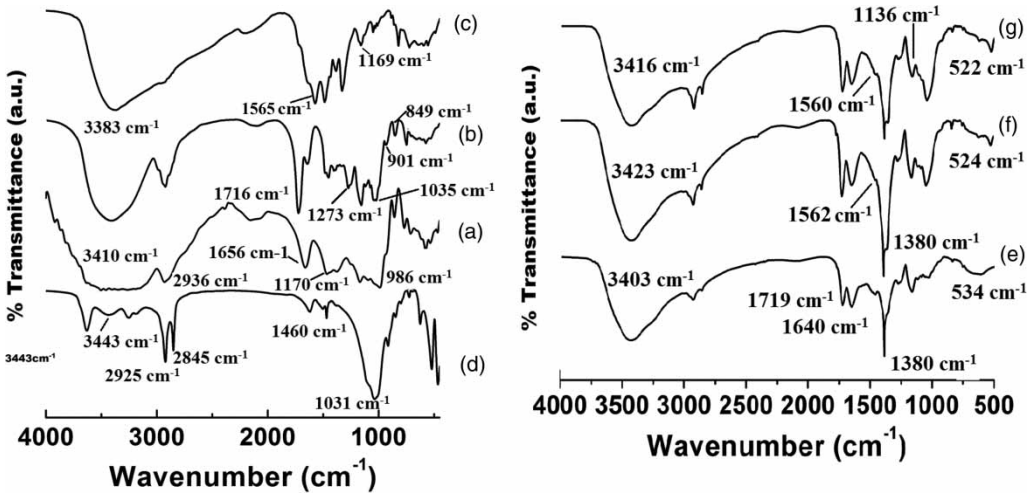

Figure 1 | FTIR spectra of (a) starch, (b) St-g-GMA, (c) AmS, (d) nanoclay (OMMT), (e) SIC, (f) SICC and (g) ATC.

The new bands at 1,565 cm^{-1} for the –NH bending vibration and at 1,169 cm^{-1} for the –CN stretching vibration had also supported the presence of amine functionality on AmS (Saikia *et al.* 2017). Again, the disappearance of the band near 1,273 cm^{-1} after amination was due to the opening up of the epoxy ring owing to new bonding of EDA with St-g-GMA moiety. In the IR spectrum of OMMT (d), characteristic bands near 3,443 and 1,460 cm^{-1} were for O–H stretching and N–H stretching respectively, while 2,925 cm^{-1} and 2,845 cm^{-1} were due to C–H stretching (Hairaldin *et al.* 2012).

Incorporation of oxyhydroxide moiety into the aminated starch to produce SIC (curve e) showed two bands near 1,640 and 1,380 cm^{-1} due to the stretching of the –COOFe group. Another band which appeared at 534 cm^{-1} was due to the stretching vibration of Fe–O. Moreover, the slight shift in the hydroxyl band towards the lower wavenumber and decreasing intensity of the amine band indicated involvement of those groups in the binding process.

Intercalation of OMMT clay in SICC (f) resulted in decreased intensity of hydroxyl and amine bands compared to those in clay and SIC. A new band near 1,031 cm^{-1} also appeared in SICC which can be attributed to Si–O linkage in clay. The decrease in intensity (Curve (g)) of bands near 1,560 and 1,136 cm^{-1} after treatment with As(III) indicated the probable interaction of it at the sorbent surface (Wang *et al.* 2012). Also, slight shifting of those characteristic bands implied a change in symmetry and hence formation of monodentate or bidentate inner sphere complexes at the sorbent surface.

The initial structures of the complexes were modeled on the basis of experimentally derived structural information. The DFT optimized geometries of the reactants arsenate oxide, arsenate hydroxide, GMA and starch (Figure 2(a)–2(d)), St-g-GMA, AmS, SICC (Figure 2(e)–2(g)) and the linkage of cross-linked compounds with arsenates are shown in Figure 2(h) and 2(i). The vibrational frequencies derived from the DFT optimized geometries are shown in Table 2 and those were found to be in good agreement with the experimental results. The geometrical parameters showing the interaction of oxides of arsenic with those of the complex are shown in Figure 2.

The bond properties (bond length) derived from the optimized geometries for arsenic adsorbed materials were found in the chemisorption range (Figure 2(i)).

Thermogravimetric analysis

The thermograms for St-g-GMA, AmS, SIC and SICC (10% clay loading) are shown in Figure 3. Thermal stability of all materials under consideration was indexed as percent weight loss at different temperatures during continuous heating. The lower the weight loss at a particular temperature, the higher is the thermal stability. Moreover, char or residue formation is also an indication of thermal stability. Higher thermal stability indicates higher resistance to loss of components entrapped within the composites and as a result the composites retain their integrity even up to very high temperature. The initial weight loss observed in St-g-GMA at around 100 °C was due to the evaporation of the small amount of water present in the sample. It was stable up to 300 °C due to grafting which is indicative of thermal stability and later continuous weight loss occurred above this temperature till 440 °C where a weight loss of about 90% occurred. This may be due to the presence of some low molecular weight compounds or some unreacted monomer in it.

The aminated starch (AmS) showed a continuous weight loss from the beginning up to 440 °C due to the decomposition of the biopolymer without crosslinking. For SIC, the initial weight loss at 100 °C was due to the presence of moisture. The major degradation took place from 190 °C and ultimately a weight loss of about 70% occurred at 500 °C. The TGA curves of the SICC with varying amounts of nanoclay loading (5, 10 and 20%) are shown in Figure 3(d)–3(f). The loading of OMMT clay into the composite exhibited very good thermal stability with 10% exhibiting the best property in all respects, while in the case of 20% clay loading thermal property deteriorated relatively. OMMT, due to its layered structure, provided resistance to the degraded volatile components to escape from the bulk. At 10% OMMT loading compounds, the delamination of clay layers may be taking place nicely resulting in a remarkable improvement in thermal stability. The interaction of OMMT clay with different components had also increased, suggesting an enhancement of thermal stability. However, at 20% OMMT loading, the agglomeration of nanoclay may have occurred and hence a decrease in thermal stability was observed. The enhanced thermal properties due to clay loading indicated good interactions among the components at the molecular level.

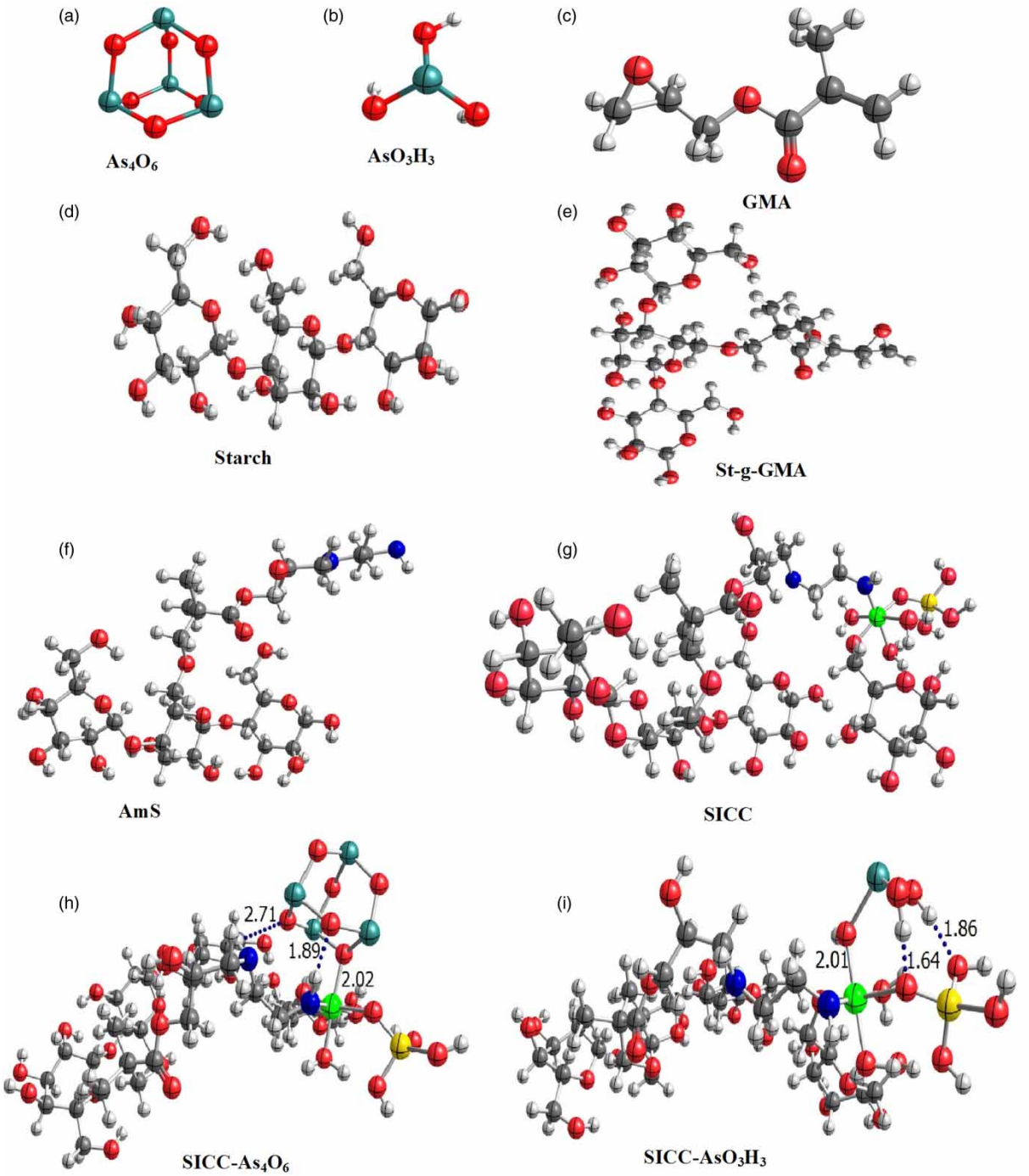

Figure 2 | Optimized geometries for different reactants and complexes.

XRD study

The characteristic peak for starch biopolymer was found to appear at $2\theta = 23°$, which is as reported earlier (Xie *et al.* 2011). Grafting with GMA resulted in the disappearance of the peak at $2\theta = 23°$ of starch, indicating loss in crystallinity due to side chain grafting. Also, two new peaks appeared at $2\theta = 17$ and $30°$. Those may have appeared because of the

Table 2 | Experimental and theoretical infrared spectral data for the optimized complexes, ν is the vibrational frequency in cm^{-1}

Assignment		Frequency (cm^{-1})	Assignment		Frequency (cm^{-1})
GMA_*1(c)*			SICC_*1(g)*		
ν(C-O) *epoxy*	Exp.	1,275.0–1,255	ν(As-O)	Exp.	522.0
	Calc.	1,280.9		Calc.	642.9
ν(C = C) *aliphatic*	Exp.	1,620.0–1,680.0	ν(Fe-O)	Exp.	524.0
	Calc.	1,670.3		Calc.	580.5
St-g-GMA_*1(e)*			SICC-As_4O_6_*1(h)*		
ν(C-O) *epoxy*	Exp.	1,272.0	ν(N-H) *amine*	Exp.	1,560.0
	Calc.	1,282.0		Calc.	1,523.4
ν(C = C) *aliphatic*	Exp.	–	ν(O-H) *Fe-water*	Exp.	1,630.0
	Calc.	–		Calc.	1,694.1
ν(C-O) *ester*	Exp.	1,035.0	ν(As-O)	Exp.	522.0
	Calc.	1,035.2		Calc.	591.8.0
ν(C = O) *carbonyl*	Exp.	1,716.0	ν(Fe-O)	Exp.	524
	Calc.	1,762.3		Calc.	530.4
AmS_*1(f)*			SICC-AsO_3H_3_*1(i)*		
ν(C-O) *epoxy*	Exp.	840.0–950.0	ν(N-H) *amine*	Exp.	1,562.0
	Calc.	–		Calc.	1,581.8
ν(C-O) *ether*	Exp.	1,035.0	ν(O-H) *Fe-water*	Exp.	1,630.0
	Calc.	1,027.6		Calc.	1,636.9
ν(N-H) *amine*	Exp.	1,565.0	ν(As-O)	Exp.	522.0
	Calc.	1,572.9		Calc.	598.5
ν(C-N) *amine*	Exp.	1,163.0	ν(Fe-O)	Exp.	524
	Calc.	1,163.3		Calc.	549.2
SICC_*1(g)*					
ν(N-H) *amine*	Exp.	1,562.0			
	Calc.	1,599.6			
ν(O-H) *Fe-water*	Exp.	1,630.0			
	Calc.	1,643.2			

rearrangement of poly glycidyl methacrylate unit formed during the course of grafting (Yan *et al.* 2014). The presence of characteristic peaks at $2\theta = 20.5$, 34, 36.4, 40.2, 50.2, 52, 59.3 and 61.4° (curve (j)) indicated the formation of the oxy-hydroxide phase of iron (III) (Zhu *et al.* 2013). When it was incorporated into grafted starch, the intensity of characteristic peaks of the former was greatly reduced due to intercalation and hence loss in crystallinity. In the XRD pattern of OMMT (curve (i)) characteristic peaks could be seen at $2\theta = 20$ and 37° (Pamplona *et al.* 2012; Das *et al.* 2014). In SICC (curve (l)), the disappearance of the characteristic peaks of OMMT indicated that either the clay layers became fully exfoliated or delaminated.

SEM/EDX analysis

Figure 4(a)–4(e) shows the SEM images of St-g-GMA, AmS, SIC, SICC and ATC respectively. After being grafted, starch particles were visibly separated from one another and agglomeration did not take place. In aminated starch (Figure 4(b)) a slight agglomeration of particles took place which may be attributed to greater amounts of

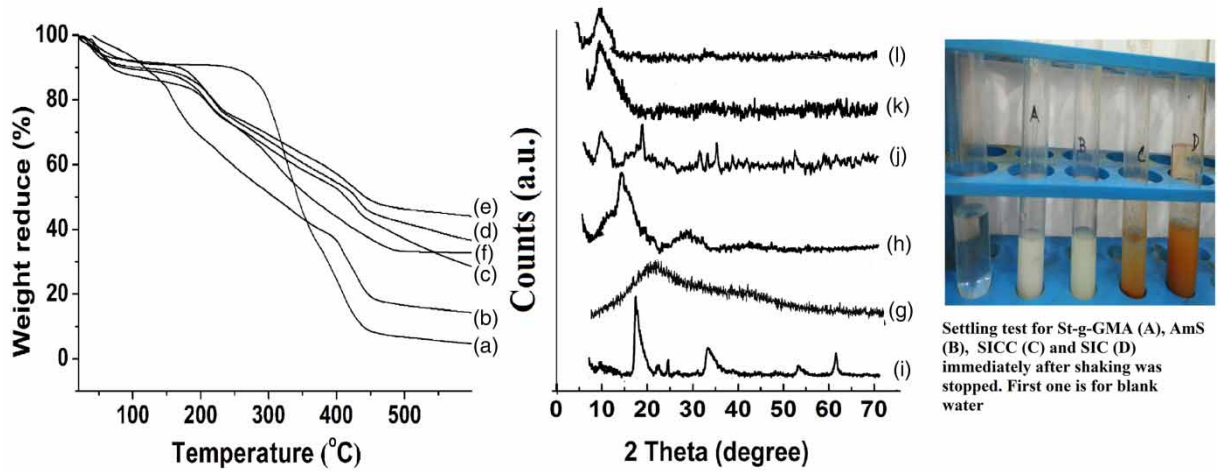

Figure 3 | TGA curves of (a) St-g-GMA, (b) AmS, (c) SIC, (d) SICC/5 (e) SICC/10, (f) SICC/20 and XRD spectra for (g) starch (h) Ams, (i) OMMT, (j) iron oxyhydroxide (k) SIC and (l) SICC/10.

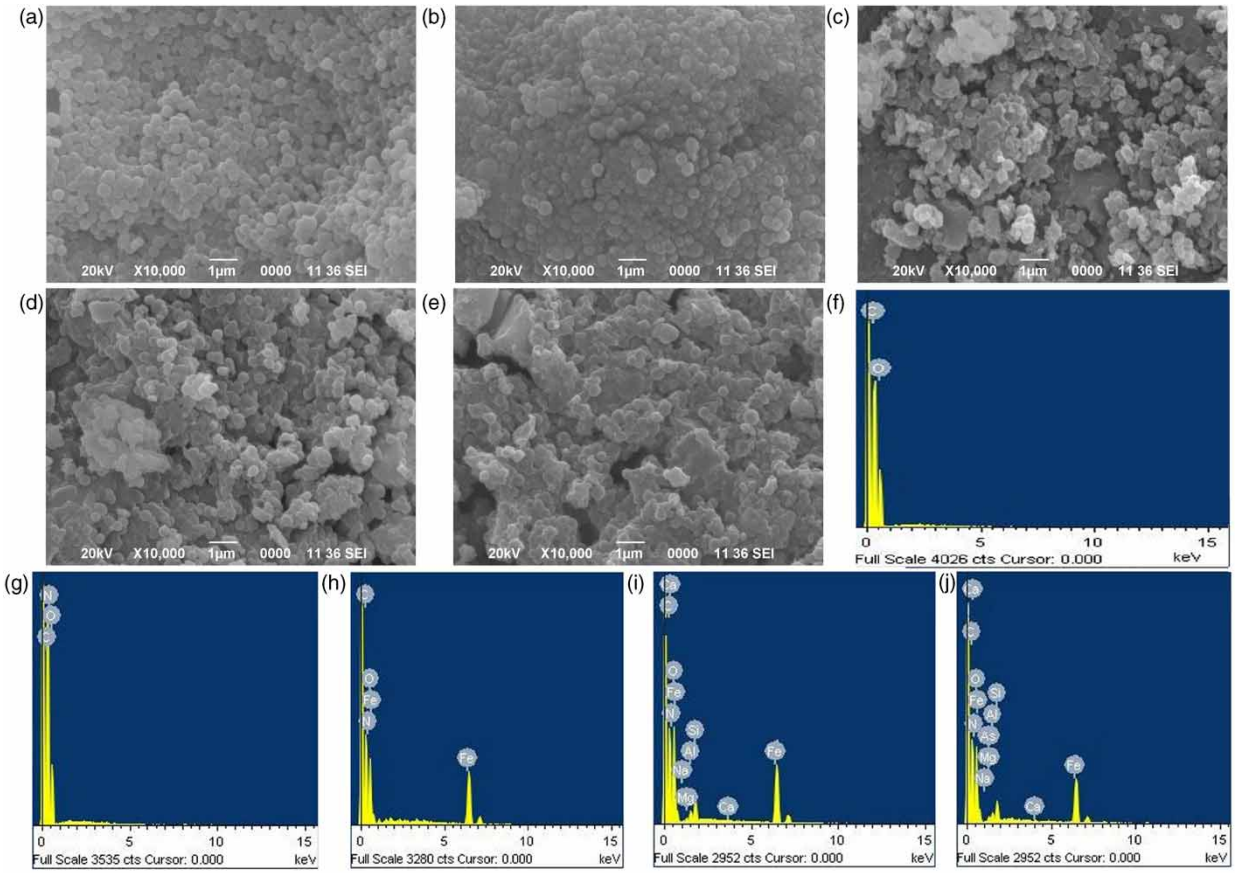

Figure 4 | (a)–(e) SEM images; (f)–(j) EDX spectra of St-g-GMA, AmS, SIC, SICC and ATC.

hydrogen bonding introduced into the system via amine functionality.

A micrograph of SIC (c) showed the formation of more agglomerated structures. Agglomeration of particles occurred due to crosslinking through oxyhydroxide moieties along with the formation of voids at sorbent surface. In the final nanocomposite (d), the surface appeared smoother and voids were partially filled as compared to (c). Incorporation of

nanoclay was responsible for such observations. Again, careful observation of surface morphology of the As(III) treated nanocomposite showed certain small particles present on the surface and the latter became comparatively smoother. This may be an indication of adsorption of As(III) on its surface.

Figure 4(f)–4(j) represents the EDX spectra of St-g-GMA, AmS, SIC, SICC and ATC respectively. In the St-g-GMA spectrum, only carbon and oxygen were observed. Elemental compositions after reacting with ethylene diamine, as represented by (g), included nitrogen along with oxygen and carbon. The presence of nitrogen along with other elements present in St-g-GMA indicated that amine functionality was successfully introduced into the system. The spectrum for SIC (h) showed additional elemental composition of iron which could be attributed to the newly incorporated oxyhydroxide system. The presence of iron, silicon, aluminum, sodium and magnesium in the EDX spectrum of SICC were due to OMMT (nanoclay). Spectra (j) suggests the sorption of arsenic on the sorbent surface.

Evaluation of efficiency of prepared materials for As(III) remediation

Comparison of efficiency of different materials

Out of all the materials prepared, the removal efficiency of oxyhydroxide and SIC were sufficiently high. Loading clay gradually enhanced the removal rate except for 20% loading. The discrepancy may be due to agglomeration occurring at higher clay concentrations. Despite significant removal capacity, oxyhydroxide alone could not be used for water treatment owing to suspended particles in the treated water. Also, clay in its pristine form merely showed any As(III) removal. However, its incorporation into SIC enhanced the removal rate owing to the synergistic influence of component materials to open up more active sites. On the basis of these observations, SICC with 10% clay loading was considered for further investigations.

Effect of material dose, treatment time and initial ion concentration

For 0.5 mg/L As(III) initial concentration, a batch experiment was carried out with a material dose ranging between 0.25 and 3 g/L of solution for 2 h (Figure 5(a)). The removal percent of arsenite initially increased rapidly and then slowly with an increasing material dose up to 2 g/L. This is the material dose which could reduce the As(III) concentration below the detection limit form the target solution. Gradual saturation of active sites on the adsorbent surface causes a lake of concentration gradient between arsenic on the adsorbent surface and that present in solution.

Effect of treatment time and initial ion concentration

Figure 5(b)–5(d) shows the effect of treatment time and initial As(III) concentration on the removal efficiency of the SICC material at three different temperatures, viz. 303, 308 and 313 K, respectively. For all temperature conditions, initially sorption was very fast, and then it showed a gradual decrease with increasing treatment time and there was hardly any increase in the removal rate beyond 60 min. This may be due to the newly established equilibrium at the adsorption surface. On the other hand, the sorption capacity of the material increased with an increase in initial ion concentration. This can be attributed to the increase in concentration gradient between As(III) ions in the two phases resulting in a shift in equilibrium towards more sorption.

Effect of temperature

The sorption capacity of the material at equilibrium increased when the temperature was increased (Figure 5(b)–5(d)). This signified the chemical nature of the sorption process. An increase in sorption at high temperature may be due to the enlargement of pore size, which increased the active surface for sorption, enhanced mobility of ions from the bulk of the solution towards the adsorbent surface. This in turn enhanced the extent of penetration within the material structure by overcoming the activation energy barrier and enhancing the rate of intraparticle diffusion (Aksu & Kabasakal 2004).

Thermodynamics and activation energy calculations

The thermodynamic data obtained for sorption of trivalent arsenic on SICC are presented in Table 3. It was noted

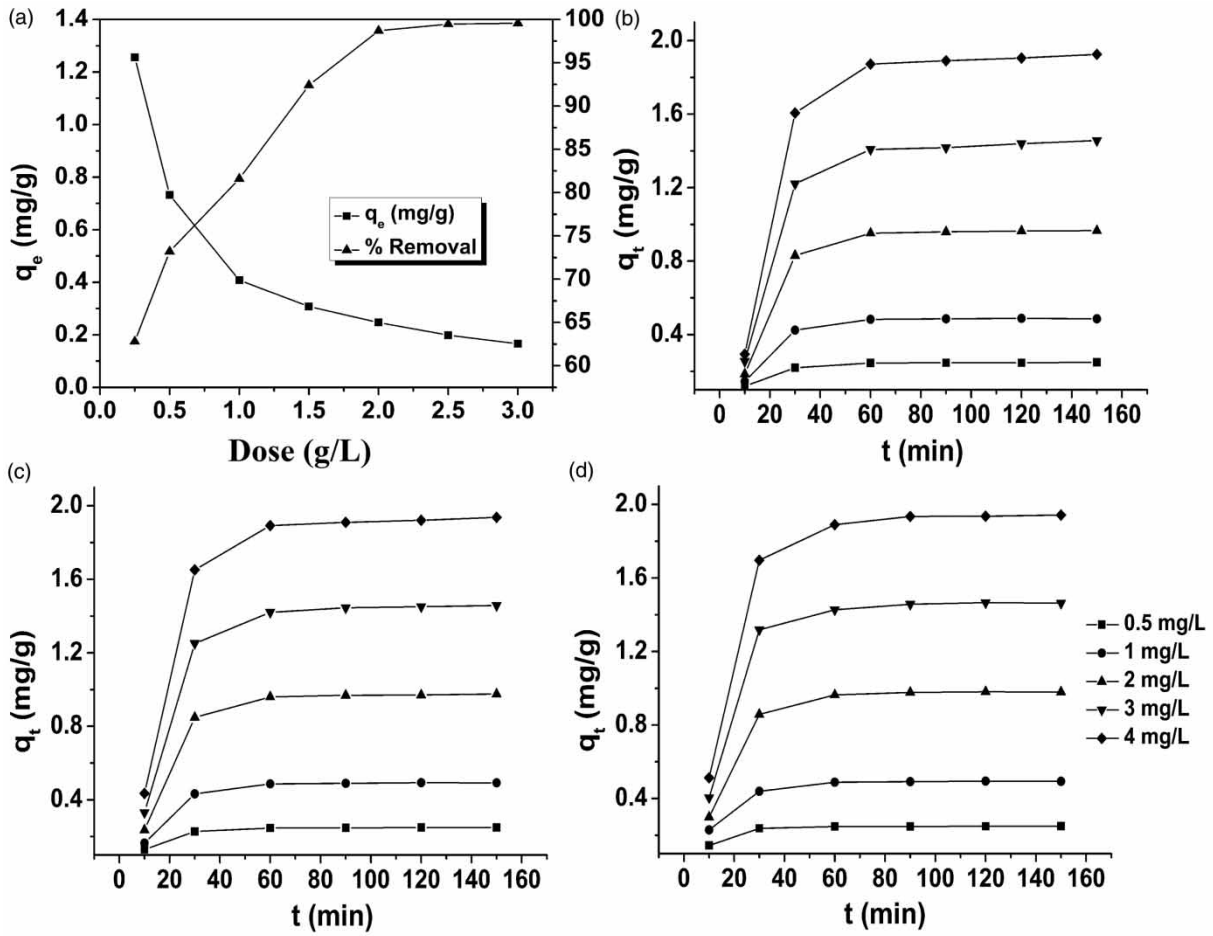

Figure 5 | Effect of material dose (a) treatment time and initial arsenic concentration at 303, 308 and 313 K (b-d) on removal efficiency of As(III).

Table 3 | Activation energy and thermodynamic parameters for sorption of As(III)

T (K)	E_a (kJmol^{-1})	K_c	R^2	ΔG° (kJ mol^{-1})	ΔH° (kJ mol^{-1})	ΔS° (J K^{-1} mol^{-1})
303	59.16	87.23	0.964	−11.25	42.48	177.6
308		125.2		−12.38		
313		149.4		−13.40		

that ΔG values were negative for all the temperatures which is in strong agreement with feasibility of the process. An increase in magnitude of ΔG with temperature implied more favorability with a rise in temperatures and hence the endothermic nature of sorption (Cantu *et al.* 2014).

The endothermic nature of sorption was further supported by a positive apparent ΔH° value (+42.48). Moreover, a high value of ΔH° (>40 kJ/mol) is an indication of chemisorption. Again, an increase in entropy at equilibrium was observed during the sorption process (+177.6). This can be attributed to an increase in molecular motion at the solid–liquid interface during the adsorption process (Wang *et al.* 2010). On the other hand, very high ΔS predicted additional molecular motion such as ion-exchange etc. Tresintsi *et al.* (2012) have established the significant role played by ion exchange due to SO_4^{2-} ions present at the surface of iron oxyhydroxide (prepared from $FeSO_4$) in acidic medium along with the formation of monodentate and bidentate inner sphere complexes for sorption of As(V). On the other hand, sorption of As(III) was explained as due to Lewis acid-base ligand-exchange reaction preferably onto non-ionized surface functional groups. Sorption of different oxyanions of arsenic on MMT and kaolinite clay was also reported by Frost & Griffin (1977). Different

mechanisms of sorption due to ion exchange were cited in this study assuming that the anion exchange sites were initially occupied by some anions such as OH^-.

Chemisorption is very specific in nature and activation energy for chemisorption is of similar magnitude to the enthalpy of a chemical reaction (Kumar 2011). The high activation energy (59.16 kJ/mol) in the presented sorption study indicated that the sorption was predominantly chemical in nature (Boparai *et al.* 2011).

Sorption kinetics

Figure 5(b)–5(d) represents the variation of q_t (mg/g) for five different initial arsenic ion concentrations in the range of 0.5–4 mg/L at varying temperatures. For each temperature q_t values increased with the increase in the initial arsenic concentrations as discussed earlier. The plots of log $(q_e - q_t)$ vs t and t/q_t vs t gave straight lines from which the different kinetic parameters for first order and second order were evaluated, as shown in Table 4.

The correlation coefficients (R^2) were computed for all the models and the values are shown in Table 4. The curve for pseudo second order kinetics exhibited a higher correlation co-efficient compared to the other models. Also, the q_e values calculated from the second order kinetic model were consistent with the experimental values. Thus, the sorption pattern could be explained more preferably by a second order kinetic model. This indicated a chemical reaction as the rate-controlling step unlike a passive diffusion process as explained by first order kinetics. At low sorbate/sorbent ratios, kinetics of sorption corresponds to a reversible second order reaction (first order at very low concentration), and two competitive reversible second order reactions at higher sorbate/sorbent ratios. Also, the linear increase in second order rate constant with increase in temperature indicated the endothermic nature of sorption.

Adsorption isotherm

Figure 6(a) shows the growth of adsorbed amount of arsenic (mg/g) at equilibrium on the surface of SICC against the increase in equilibrium concentrations. To establish the influence of arsenic concentration on the adsorption process, the equilibrium data was analyzed by linear forms of Langmuir and Freundlich equations and all the isotherm parameters observed are listed in Table 5. Also, q_e vs C_e showed linearity of the graph (Figure 6(a)).

The R^2 values for both Langmuir and Freundlich models showed good co-relations of the data and the sorption could be reasonably explained by the models under consideration. The R^2 values for Langmuir model were higher than those of the Freundlich model in the concentration range of interest. Thus, the preferential order for sorption among these

Table 4 | Parameters of different kinetic models on sorption of As(III)

		Pseudo-first-order model			Pseudo-second-order model			
Adsorption condition	**q_e, exp (mg/g)**	**k_1 (min^{-1})**	**q_e, cal (mg/g)**	**R^2**	**k_2 g/mg/min**	**q_e, cal (mg/g)**	**R^2**	**H**
Conc[a]/mgL^{-1}								
0.5	0.254	0.025	0.074	0.758	0.465	0.26	0.997	0.032
1.0	0.488	0.034	0.154	0.699	0.110	0.56	0.984	0.034
2.0	0.968	0.029	0.353	0.763	0.026	1.11	0.902	0.039
3.0	1.450	0.031	0.820	0.893	0.015	1.69	0.943	0.052
4.0	1.934	0.034	1.061	0.880	0.008	2.26	0.942	0.060
Temp[b]/K								
303	0.968	0.029	0.353	0.763	0.026	1.11	0.902	0.039
308	0.976	0.031	0.382	0.783	0.039	1.16	0.954	0.053
313	0.980	0.038	0.458	0.862	0.056	1.22	0.995	0.069

[a]Conditions: temp. 30 °C, material dose 2 g/L.
[b]Conditions: concentration 2 g/L, material dose 2 g/L.

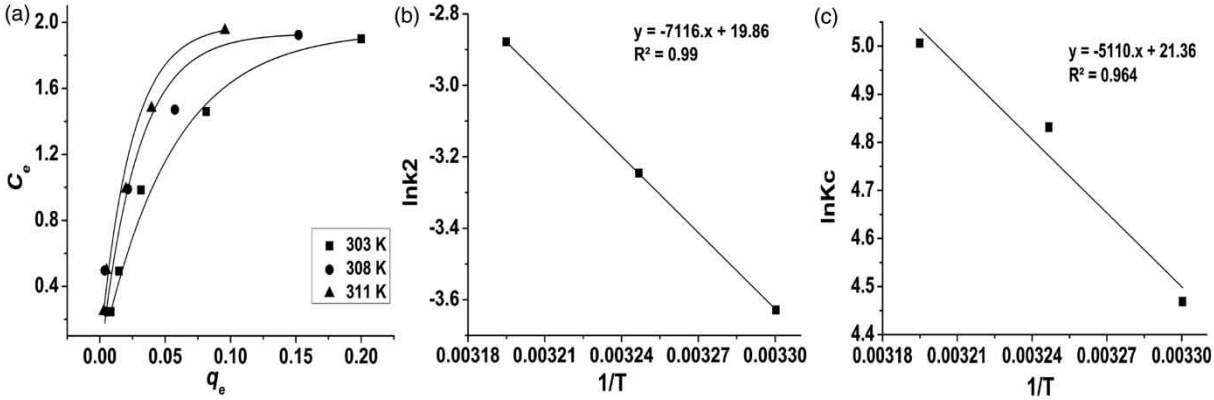

Figure 6 | (a) Isotherm plot; (b) Arrhenius plot; and (c) thermodynamic plot of sorption of As(III) on SICC at three different temperatures.

Table 5 | Isotherm constants and correlation coefficients for sorption of As(III)

	Langmuir parameters			Freundlich parameters		
T/K	q_m (mg/g)	R_L	R^2	K_F (mg/g)	N	R^2
303	2.04	0.081	0.973	6.37	1.59	0.896
308	2.29	0.133	0.977	5.54	1.92	0.925
313	2.43	0.095	0.991	8.52	1.76	0.961

models is as follows: Langmuir > Freundlich. This supports the chemical nature of the sorption.

CONCLUSION

The combined system of aminated starch, organoclay and oxyhydroxide was found to be an efficient material for trivalent arsenic remediation. The oxyhydroxide acted as a good cross-linking agent and also took part in As(III) sorption. Different analytical tools confirmed all the possible interactions during the preparation of destined material and its successful implication in the sorption of As(III). Incorporation of an optimum amount of clay (10%) further contributed to the sorption process. The sorption process was spontaneous, governed by a pseudo second order kinetic model. The value of ΔH and activation energy confirmed the chemical nature of the sorption.

These findings have opened up many significant prospects of starch and iron oxyhydroxide and clay minerals for water treatment. Starch has never been reported alone as a sorbent for water contaminants. Iron oxyhydroxide has a high affinity for arsenic but its stability in water is questionable and gets easily deteriorated. However, for water treatment, process stability of sorbent material and hence its reusability is most important. Besides the surface functionality and ion exchange capability, monitoring and manipulating the separation among intercalated clay layers may be helpful for selective sorption of contaminants from water. The study of the pH affect and exact mechanism of sorption may open up numerous opportunities to further upgrade the material or synthesizing new materials which can open up scope to devise them for end use application.

ACKNOWLEDGEMENT

The authors are grateful to the Central University Tezpur for technical support.

DATA AVAILABILITY STATEMENT

All relevant data are included in the paper or its Supplementary Information.

REFERENCES

Adeleye, A. S., Conway, J. R., Garner, K., Huang, Y., Su, Y. & Keller, A. A. 2016 Engineered nanomaterials for water treatment and remediation: costs, benefits, and applicability. *Chem. Eng. Sci.* **286**, 640–662.

Aksu, Z. & Kabasakal, E. 2004 Batch adsorption of 2, 4-dichlorophenoxy-acetic acid (2, 4-D) from aqueous solution by granular activated carbon. *Sep. Purif. Technol.* **35**, 223–240.

Appalakondaiah, S., Vaitheeswaran, G., Lebegue, S., Christensen, N. E. & Svane, A. 2012 Effect of van der Waals interactions on the structural and elastic properties of black phosphorus. *Phys. Rev. B: Condens. Matter* **86**, 035105.

Banu, H. T., Karthikeyan, P. & Meenakshi, S. 2018 Lanthanum (III) encapsulated chitosan-montmorillonite composite for the adsorptive removal of phosphate ions from aqueous solution. *Int. J. Biol. Macromol.* **112**, 284–293.

Boparai, H. K., Joseph, M. & O'Carroll, D. M. 2011 Kinetics and thermodynamics of cadmium ion removal by adsorption onto nano zerovalent iron particles. *J. Hazard. Mater.* **186**, 458–465.

Cantu, Y., Remes, A., Reyna, A., Martinez, D., Villarreal, J., Ramos, H., Trevino, S., Tamez, C., Martinez, A., Eubanks, T. & Parsons, J. G. 2014 Thermodynamics, kinetics, and activation energy studies of the sorption of chromium (III) and chromium (VI) to a mn3o4 nanomaterial. *Chem. Eng. J.* **254**, 374–383.

Catalano, J. G., Luo, Y. & Otemuyiwa, B. 2011 Effect of aqueous Fe (II) on arsenate sorption on goethite and hematite. *Environ. Sci. Technol.* **45**, 8826–8833.

Cheira, M. F., Rashed, M. N., Mohamed, A. E., Hussein, G. M. & Awadallah, M. A. 2019 Removal of some harmful metal ions from wet-process phosphoric acid using murexide-reinforced activated bentonite. *Mater. Today Chem.* **14**, 100176.

Cumbal, L. & Sen Gupta, A. K. 2005 Arsenic removal using polymer-supported hydrated iron (III) oxide nanoparticles: role of Donnan membrane effect. *Environ. Sci. Technol.* **39**, 6508–6515.

Das, G., Kalita, R. D., Gogoi, P., Buragohain, A. K. & Karak, N. 2014 Antibacterial activities of copper nanoparticle-decorated organically modified montmorillonite/epoxy nanocomposites. *Appl. Clay Sci.* **90**, 18–26.

Delley, B. 1990 An all-electron numerical method for solving the local density functional for polyatomic molecules. *J. Chem. Phys.* **92**, 508–517.

Delley, B. 1998 A scattering theoretic approach to scalar relativistic corrections on bonding. *Int. J. Quantum Chem.* **69**, 423–433.

Delley, B. 2000 From molecules to solids with the DMol 3 approach. *J. Chem. Phys.* **113**, 7756–7764.

Frost, R. R. & Griffin, R. A. 1977 Effect of pH on adsorption of arsenic and selenium from landfill leachate by clay minerals. *Soil Sci. Soc. Am. J.* **41**, 53–57.

Gogoi, P., Adhikari, P. & Maji, T. K. 2017a Bioremediation of arsenic from water with citric acid cross-linked water hyacinth (*E. crassipes*) root powder. *Environ. Monit. Assess.* **189**, 1–11.

Gogoi, P., Dutta, D. & Maji, T. K. 2017b Equilibrium and kinetics study on removal of arsenate ions from aqueous solution by CTAB/TiO_2 and starch/CTAB/TiO_2 nanoparticles: a comparative study. *J. Water Health* **15**, 58–71.

Gogoi, P., Thakur, A. J., Devi, R. R., Das, B. & Maji, T. K. 2017c Adsorption of As (V) from contaminated water over chitosan coated magnetite nanoparticle: equilibrium and kinetics study. *Environ. Nanotechnol. Monit. Manag.* **8**, 297–305.

Hairaldin, S. Z., Wan Yunus, W. M. Z. & Ibrahim, N. A. 2012 Effect addition of octadecylamine modified clay (ODA-MMT) to polylactide/polycaprolactone (PLA/PCL) blend. *Advanced Materials Research* **364**, 317–321.

Hasan, S., Ghosh, A., Race, K., Schreiber Jr, R. & Prelas, M. 2014 Dispersion of FeOOH on chitosan matrix for simultaneous removal of As (III) and As (V) from drinking water. *Sep. Sci. Technol.* **49**, 2863–2877.

Hedin, J., Östlund, Å. & Nydén, M. 2010 UV induced cross-linking of starch modified with glycidyl methacrylate. *Carbohydr. Polym.* **79**, 606–613.

Hristovski, K., Baumgardner, A. & Westerhoff, P. 2007 Selecting metal oxide nanomaterials for arsenic removal in fixed bed columns: from nanopowders to aggregated nanoparticle media. *J. Hazard. Mater.* **147**, 265–274.

Khodabakhshi, A., Amin, M. M. & Mozaffari, M. 2011 Synthesis of magnetite nanoparticles and evaluation of its efficiency for arsenic removal from simulated industrial wastewater. *Iran. J. Environ. Health Sci. Eng.* **8**, 189–200.

Kousalya, G. N., Gandhi, M. R. & Meenakshi, S. 2010 Sorption of chromium (VI) using modified forms of chitosan beads. *Int. J. Biol. Macromol.* **47**, 308–315.

Kumar, U. 2011 Thermodynamics of the adsorption of Cd (II) from aqueous solution on NCRH. *Int. J. Environ. Sci. Technol.* **2**, 334–336.

Kumar, A. S. K., Kalidhasan, S., Rajesh, V. & Rajesh, N. 2012 Application of cellulose-clay composite biosorbent toward the effective adsorption and removal of chromium from industrial wastewater. *Ind. Eng. Chem.* **51**, 58–69.

Lenoble, V., Bouras, O., Deluchat, V., Serpaud, B. & Bollinger, J. C. 2002 Arsenic adsorption onto pillared clays and iron oxides. *J. Colloid Interface Sci.* **255**, 52–58.

Lenoble, V., Deluchat, V., Serpaud, B. & Bollinger, J. C. 2003 Arsenite oxidation and arsenate determination by the molybdene blue method. *Talanta* **61**, 267–276.

Li, Z. & Bowman, R. S. 2001 Retention of inorganic oxyanions by organo-kaolinite. *Water Res.* **35**, 3771–3776.

Mohapatra, D., Mishra, D., Chaudhury, G. R. & Das, R. P. 2007 Arsenic adsorption mechanism on clay minerals and its dependence on temperature. *Korean J. Chem. Eng.* **24**, 426–430.

Ortmann, F., Bechstedt, F. & Schmidt, W. G. 2006 Semiempirical van der Waals correction to the density functional description of solids and molecular structures. *Phys. Rev. B Condens. Matter* **73**, 205101.

Pamplona, T. F., Amoni, B. D. C., Alencar, A. E. V. D., Lima, A. P. D., Ricardo, N. M., Soares, J. B. & Soares, S. D. A. 2012 Asphalt binders modified by SBS and SBS/nanoclays: effect on rheological properties. *J. Braz. Chem. Soc.* **23**, 639–647.

Perdew, J. P., Burke, K. & Wang, Y. 1996 Generalized gradient approximation for the exchange-correlation hole of a many-electron system. *Phys. Rev. B Condens. Matter* **54**, 16533.

Saikia, C., Das, M. K., Ramteke, A. & Maji, T. K. 2017 Evaluation of folic acid tagged aminated starch/ZnO coated iron oxide nanoparticles as targeted curcumin delivery system. *Carbohydr. Polym.* **157**, 391–399.

Santhosh, C., Velmurugan, V., Jacob, G., Jeong, S. K., Grace, A. N. & Bhatnagar, A. 2016 Role of nanomaterials in water treatment applications: a review. *J. Hazard. Mater.* **306**, 1116–1137.

Sepehri, A. & Sarrafzadeh, M. H. 2018 Effect of nitrifiers community on fouling mitigation and nitrification efficiency in a membrane bioreactor. *Chem. Eng. Process.* **128**, 10–18.

Srinivasan, R. 2011 Advances in application of natural clay and its composites in removal of biological, organic, and inorganic contaminants from drinking water. *Adv. Mater. Sci. Eng.* **2011**, 1–17.

Tresintsi, S., Simeonidis, K., Vourlias, G., Stavropoulos, G. & Mitrakas, M. 2012 Kilogram-scale synthesis of iron oxy-hydroxides with improved arsenic removal capacity: study of Fe (II) oxidation–precipitation parameters. *Water Res.* **46**, 5255–5267.

Uddin, M. K. 2017 A review on the adsorption of heavy metals by clay minerals, with special focus on the past decade. *Chem. Eng. Sci.* **308**, 438–462.

Vitela-Rodriguez, A. V. & Rangel-Mendez, J. R. 2013 Arsenic removal by modified activated carbons with iron hydro (oxide) nanoparticles. *J. Environ. Manage.* **114**, 225–231.

Wang, L., Zhang, J., Zhao, R., Li, C., Li, Y. & Zhang, C. 2010 Adsorption of basic dyes on activated carbon prepared from Polygonum orientale Linn: equilibrium, kinetic and thermodynamic studies. *Desalination* **254** (1–3), 68–74.

Wang, X., Guo, Y., Yang, L., Han, M., Zhao, J. & Cheng, X. 2012 Nanomaterials as sorbents to remove heavy metal ions in wastewater treatment. *J. Environ. Anal. Toxicol.* **2** (7), 154–158.

Xie, G., Shang, X., Liu, R., Hu, J. & Liao, S. 2011 Synthesis and characterization of a novel amino modified starch and its adsorption properties for Cd (II) ions from aqueous solution. *Carbohyd. Polym.* **84** (1), 430–438.

Yan, X., Li, M., Long, J., Zhang, X., Wei, H., He, Q., Rutman, D., Cao, D., Wei, S., Chen, G. & Guo, Z. 2014 Highly monodisperse sub-microspherical poly (glycidyl methacrylate) nanocomposites with highly stabilized gold nanoparticles. *Macromol. Chem. Phys.* **215**, 1098–1106.

Zhao, X., Lv, L., Pan, B., Zhang, W., Zhang, S. & Zhang, Q. 2011 Polymer-supported nanocomposites for environmental application: a review. *Chem. Eng. J.* **170**, 381–394.

Zhou, J., Xiao, F., Wang, W. N. & Fan, K. N. 2007 Theoretical study of the interaction of nitric oxide with small neutral and charged silver clusters. *J. Mol. Struct. Theochem.* **818**, 51–55.

Zhu, W., Nan, Y., Huang, T. & Wu, F. 2013 The mechanism, thermodynamic and kinetic characteristics of the microbial reduction of goethite mediated by anthraquinone-2-sulfonate. *Geomicrobiol. J.* **30**, 928–940.

Zubair, M., Jarrah, N., Khalid, A., Manzar, M. S., Kazeem, T. S. & Al-Harthi, M. A. 2018 Starch-NiFe-layered double hydroxide composites: efficient removal of methyl orange from aqueous phase. *J. Mol. Liq.* **249**, 254–264.

First received 16 November 2020; accepted in revised form 16 February 2021. Available online 25 March 2021